phonon dispersion with the resolution of a two-axis spectrometer. An alternative approach consists in measuring TDS-free data, as proposed, for example, by Jex, Müllner, Knoth & Loidl (1980) for KCN using Mössbauer diffraction or alternatively using a spin-echo triple-axis spectrometer with an extremely good energy resolution (Hayter, Lehmann, Mezei & Zeyen, 1979). The important influence of TDS on the measured intensities may also be concluded from the fact that the values of $\langle u^2 \rangle$ found in this paper are only about half the values derived from the lattice dynamical model mentioned above (Ehrhardt, 1981). It is well known that the intensity of high-indexed reflections is increased due to TDS and this causes values of $\langle u^2 \rangle$ which are systematically too low.

There is another remark concerning the mean-squared amplitudes: they change little between 300 and 150 K and hence considerably less than expected from the normal behaviour, namely $\langle u^2 \rangle \simeq T$. This is in agreement with investigations on KCN and with the predictions of the lattice dynamical model (Ehrhardt, 1981). The probable origin of this finding is the behaviour of the soft elastic constant c_{44}, which decreases with decreasing temperature and gives increasing mean-squared amplitudes. It should be remarked that the method used gives reliable CN bond lengths (see Table 2).

The authors are indebted to S. Haussühl who kindly supplied us with the RbCN single crystal and they thank K. H. Michel for discussions.

References

BLEIF, H. J. (1978). *Kristalline Phasen und Phasenübergänge von* NaOH. PhD Thesis, Univ. Tübingen.

DOLLING, G., POWELL, B. M. & SEARS, V. F. (1979). *Mol. Phys.* **37**, 1859–1883.

DULTZ, W. & KRAUSE, H. (1978). *Phys. Rev. B*, **18**, 394–400.

DULTZ, W., OTTO, H. H., KRAUSE, H. & BUEVOZ, J. L. (1981). *Phys. Rev. B*, **24**, 1287–1291.

EHRHARDT, K.-D. (1981). Report JÜL-1713. Kernforschungsanlage Jülich.

EHRHARDT, K.-D., PRESS, W., LEFEBVRE, J. & HAUSSÜHL, S. (1980). *Solid State Commun.* **34**, 591–593.

HAUSSÜHL, S. (1973). *Solid State Commun.* **13**, 147–151.

HAYTER, J. B., LEHMANN, M. S., MEZEI, F. & ZEYEN, C. M. W. (1979). *Acta Cryst.* A**35**, 333–336.

HEGER, G., MASSING, S., GUTH, H., REIMERS, W. & PAULUS, H. (1981). Report KfK 3213. Kernforschungszentrum Karlsruhe.

JEX, H., MÜLLNER, M., KNOTH, R. & LOIDL, A. (1980). *Solid State Commun.* **36**, 713–716.

KARA, M. (1982). *Acta Cryst.* A**38**, 274–285.

KARA, M. & KURKI-SUONIO, K. (1981). *Acta Cryst.* A**37**, 201–210.

KONDO, Y., SHOEMAKER, D. & LÜTY, F. (1979). *Phys. Rev. B*, **19**, 4210–4216.

KURKI-SUONIO, K. (1967). *Ann. Acad. Sci. Fenn. Ser. A*4, pp. 241–263.

MICHEL, K. H. & NAUDTS, J. (1977). *J. Chem. Phys.* **67**, 547–558.

PARRY, G. S. (1962). *Acta Cryst.* **15**, 601–607.

PRESS, W., GRIMM, H. & HÜLLER, A. (1979). *Acta Cryst.* A**35**, 881–885.

PRESS, W. & HÜLLER, A. (1973). *Acta Cryst.* A**29**, 252–256.

ROWE, J. M., HINKS, D. G., PRICE, D. L., SUSMAN, S. & RUSH, J. J. (1973). *J. Chem. Phys.* **58**, 2039–2042.

ROWE, J. M., RUSH, J. J., VAGELATOS, N., PRICE, D. L., HINKS, D. G. & SUSMAN, S. (1975). *J. Chem. Phys.* **62**, 4551–4554.

SEYMOUR, R. S. & PRYOR, A. W. (1970). *Acta Cryst.* B**26**, 1487–1491.

WILLIS, B. T. M. & PRYOR, A. W. (1975). *Thermal Vibrations in Crystallography*. Cambridge Univ. Press.

Acta Cryst. (1983). B**39**, 175–185

The Chemical Bonding in Lithium Metaborate, $LiBO_2$. Charge Densities and Electrostatic Properties

BY A. KIRFEL AND G. WILL

Mineralogisches Institut der Universität Bonn, Lehrstuhl für Mineralogie und Kristallographie, Poppelsdorfer Schloss, D-5300 Bonn 1, Federal Republic of Germany

AND R. F. STEWART

Carnegie–Mellon University, Department of Chemistry, 4400 Fifth Avenue, Pittsburgh, PA 15213, USA

(*Received 5 July* 1982; *accepted 15 November* 1982)

Abstract

The room-temperature electron density distribution in $LiBO_2$ has been studied by X-ray diffraction experiments up to $s = 1{\cdot}08$ Å^{-1}. Conventional structure refinements both with HF scattering factors for the neutral atoms and with the monopole parts of generalized scattering factors (GSF) calculated from the diatomic-molecule wavefunctions of LiO and BO yielded $R_w^{HF} = 0{\cdot}0251$ and $R_w^{GSF} = 0{\cdot}0192$ for 1266 observed reflections. The data were also used for high-order refinements with various cut-off angles in

0567-7408/83/020175-11$01.50

order to assess positional and vibrational parameters least biased by bonding effects as well as to estimate the scale factor. Rigid pseudoatom model multipole expansions up to fourth-order refinements have been employed. The final agreement factors, $R_w^{HF} = 0.0047$ and $R_w^{GSF} = 0.0046$, represent a drastic improvement of the models, which both yielded essentially identical results. Parameters based on the HF monopoles were used for calculations of dynamic and static deformation density, deformation potential, and deformation electric field distributions in interesting sections of the structure. These are discussed in terms of the information about bond-induced charge redistribution in $LiBO_2$ and of the theoretical deformation density distributions of the diatomic systems. Common features in the experimentally derived and the theoretical maps lead to a simple model of chemical bonding in the '$LiBO_2$ molecule' and of the polymerization of these units to form endless chains of BO_3 triangles held together by electrostatic forces. The charge character of the Li atom is indicated to be onefold positive by all relevant results. [Crystal data: $M_r = 49.748$, $P2_1/c$, $a = 5.845$ (1), $b = 4.353$ (1), $c = 6.454$ (1) Å, $\beta = 115.09$ (1)°, $V = 148.72$ (4) Å^3, $Z = 4$.]

Introduction

The crystal structure of lithium metaborate, $LiBO_2$, was first investigated by Zachariasen (1964). Based on 198 unique reflections of equal weight, measured on a single-crystal diffractometer, the author refined the structure to $R = 0.046$ (0.041 omitting unobserveds) with neutral-atom form factors. The structure (Fig. 1) contains endless chains of BO_3 triangles as in $Ca(BO_2)_2$ (Marezio, Plettinger & Zachariasen, 1963*a*). These chains are parallel to **b**, and the atoms of a chain are almost coplanar, parallel to (10$\bar{5}$). The Li atom also lies approximately in the same layer, and is fivefold coordinated by O atoms. There are three Li–O 'bonds' within one chain and one 'bond' with each of the two neighbouring chains. Zachariasen (1963, 1964) suggested that the O(1) atom, being bonded to two B atoms and to one Li atom, is 'overbonded', whereas O(2), forming one B–O bond and four Li–O 'bonds', is 'underbonded'. This imbalance served as an explanation for the observed differences in the B–O bond lengths, *e.g.* a lengthening (weakening) of the B–O(1) bonds and a strengthening of the B–O(2) bond.

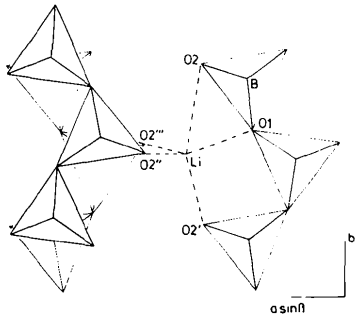

Fig. 1. Projection of the crystal structure of $LiBO_2$ on (001).

The progress in chemical-bond studies by means of X-ray diffraction experiments and ensuing evaluations of electron density distributions and of electrostatic properties enables us to look closer into the bonding in $LiBO_2$. The main question concerns the nature of the interaction between the Li and O atoms, *e.g.* are there directed Li–O bonds or is the crystal held together predominantly by electrostatic forces between Li^+ and $[BO_2]_\infty^{-\infty}$ chains? The covalent B–O bonds and the formal charge characters of these atoms are also of interest. Furthermore, $LiBO_2$ is very well suited for electron density studies, since there are only 8 core electrons but 16 valence electrons per formula unit. This can be expressed by the suitability factor (Stevens & Coppens, 1976)

$$S = V(Z\sum n_{core}^2)^{-1} = 2.32$$

(V = unit-cell volume, Z = number of formula units/cell, n = number of core electrons) compared to 1.85 for the previously studied $B_{13}C_2$ (Kirfel, Gupta & Will, 1979).

Since S represents an inverse-squared core-electron concentration, bonding effects in the observable electron distribution can be expected to be the more prominent the greater the S value. Another favourable property of $LiBO_2$ is the high melting point of 1118 K, which precludes the need for performing the measurements at low temperatures. These circumstances led to the expectation of detecting significant bonding effects in the electron distribution in $LiBO_2$ and of an improved bonding model derived from experimental evidence.

Experimental

Colourless, needle-shaped crystals were obtained from the melt by Behm (1976). For the X-ray diffraction experiments an untwinned specimen (checked by Weissenberg photographs) was selected. The diffraction data were collected on an automatic four-circle diffractometer (Syntex $P2_1$) with Mo $K\alpha$ radiation and a graphite monochromator ($2\theta_m = 12.2°$). The unit-cell parameters were determined by least-squares methods from the angular settings of 25 reflections with $2\theta > 30°$. Table 1 shows the crystallographic data for $LiBO_2$ and Table 2 details of data collection. The total background counting time equalled the time spent for the peak count. In the course of the data reduction the intensities were first adjusted to the fluctuations of the sums of the standard reflection intensities. After Lp correction, including consideration of the polarization of

Table 1. *Crystallographic data for* $LiBO_2$

	This work	Zachariasen (1964)
a_o (Å)	5·845 (1)	5·838 ± 0·002
b_o (Å)	4·353 (1)	4·348 ± 0·001
c_o (Å)	6·454 (1)	6·449 ± 0·002
β (°)	115·09 (1)	115·12 ± 0·02
V (Å^3)	148·72 (4)	148·21
Space group	$P2_1/c$	$P2_1/c$
M_r	49·748	49·748
Z	4	4
D_x (Mg m^{-3})	2·21	2·223
D_m (Mg m^{-3})		2·18
μ (Mo $K\alpha$) (mm^{-1})	0·213	

Table 2. *Data collection and processing*

Wavelength	0·71069 Å
Crystal dimensions	0·35 × 0·20 × 0·10 mm
Maximum θ	50°
$(\sin\theta/\lambda)_{max}$	1·078 Å^{-1}
Scan mode	θ–2θ step scan
Number of steps/reflection	96
Scan angle	2·0° plus (α_1,α_2)°
Scan speed	1·0–10·0° min^{-1}
Number of check reflections	6
Check-reflection interval	28
Number of reflections recorded	7339
Number of unique reflections	1366
Number of unobserved reflections	140 ($I < 1·5\sigma$)
Internal match, R_{int}	0·023

the primary beam, symmetry-related reflections were averaged. No absorption correction was applied, but an estimate of maximum error $|\Delta F/F|$ is 1·3%. The internal match of the data set based on an unweighted

$$R_{\rm Int} = \sum_l \sum_j |\bar{I}_l - I_{l,j}| / \sum_l \sum_j I_{l,j} = 0{\cdot}023$$

demonstrates the good quality of the data.

Data analysis

(*a*) *Independent-atom (IA) refinements*

The positional and thermal parameters reported by Zachariasen (1964) were taken as starting values for conventional least-squares refinements with reflections weighted with their own σ's [$w = 1/\sigma^2(F)$] based on counting statistics.

(i) HFIAM: the scattering factors of the neutral atoms B, O and Li as well as of Li^+ were calculated from the Hartree–Fock wavefunctions given by Clementi (1965). The electron populations $p_{\rm core}$ were set to 5, 8, 3 or 2 respectively.

(ii) GSFIAM: monopole scattering factors were derived from accurate wavefunctions of the diatomic systems B—O for B and O, and Li–O for Li (Cade & Huo, 1975), both expanded to the [4/4] level. The general method has been reported previously (Stewart, Bentley & Goodman, 1975; Bentley & Stewart, 1976). These expansions yielded zero moments, *i.e.* charge values of Li: 2·03344, B: 4·08475, and O: 8·9152 (Spackman & Stewart, 1982). These core populations and the modified shapes of the $f(h)_{p,\rm core}$ functions already expressed some charge redistribution due to the bonding. Thus it should be noted that the model contains spherical atoms rather than truly independent atoms. The agreement factors $R_{\rm o.u.}$ (o.u. = omitting unobserveds) and $R_{w.o.u.}$ (w = weighted) obtained from full-matrix least-squares refinements of the scale factor, and of the positional and vibrational parameters were HFIAM: $R_{\rm o.u.}$ = 0·0392 ($R_{w.o.u.}$ = 0·0251) and GSFIAM: 0·0296 (0·0192) (see Table 3), indicating the GSFIAM model to be significantly better than the HFIAM at the IAM level.

No further improvement was obtained by inclusion of an isotropic-extinction coefficient (Becker & Coppens, 1974*a*,*b*) in the list of variables, and therefore extinction was considered negligible, *i.e.* kinematic diffraction theory was assumed adequate for the analysis.

The positional and especially the thermal parameters derived from all data refinements of light-atom structures can be affected considerably by the redistribution of the valence electrons due to bonding. The correlation between the first and again especially the second cumulants and the scale factor k then also affects this variable. However, the scattering contributions of the delocalized electron distributions become very small – as a rule of thumb, beyond 0·7 Å^{-1} in reciprocal space. The structure amplitudes observed at high diffraction

Table 3. *Refinement results*

	HFIAM(Li^+)	HFIAM(Li) GSFIAM	HF–HO GSF–HO	HFM-1 GSFM-1	HFM-2 GSFM-2	HFM-3 GSFM-3	HFM-4 GSFM-4
$R_{\rm o.u.}$	0·0396	0·0392 0·0296	0·0261 0·0261	0·0273 0·0271	0·0163 0·0161	0·0153 0·0150	0·0148 0·0146
$R_{w.o.u.}$	0·0307	0·0251 0·0192	0·0123 0·0123	0·0169 0·0170	0·0060 0·0056	0·0051 0·0049	0·0047 0·0046
GOF	12·02	11·82 9·05	1·65 1·65	7·78 7·91	2·94 2·64	2·39 2·29	2·21 2·18
Scale	1·078 (2)	1·080 (2) 1·056 (8)	1·000 (4) 1·005 (4)	1·06 (2) 1·05 (2)	1·04 (1) 0·98 (1)	1·03 (1) 0·97 (1)	1·05 (1) 1·01 (1)

In all multipole refinements the scale was estimated from: $k = (\Sigma_{\rm syn} \Sigma_p \Sigma C_{p0})/F(000)$.

angles are almost exclusively determined by the core electrons, localized close to the nuclei. Therefore, refinements employing both HFIAM and GSFIAM were also carried out with 'high-order (HO)' data at increasing cut-off angles. These refinements were presumed, at best, to determine atomic parameters unbiased by bonding effects, and to establish a reliable estimate of the scaling (k) between the relative observed (though prescaled) and the absolute calculated structure amplitudes.

Fig. 2 shows the dependencies of the refined scale factors and of the agreement factors (HFIAM) on the HO cut-off angle taken in steps of 0·05 Å^{-1} in $\sin\theta/\lambda$ (s). The observed differences in k of about 8% (HFIAM) and 5·5% (GSFIAM) between the all-data refinements and the HO refinements at $s = 0{\cdot}8$ Å^{-1} are in agreement with earlier experiences (Stevens & Coppens, 1975; Kirfel *et al.*, 1979) and show impressively the correlation problem. The lower scale factor from GSFIAM and its smoother decrease with increasing cut-off angle indicate again the superiority of the generalized scattering factors at this stage of analysis. At $s = 0{\cdot}8$ Å^{-1} and beyond virtually identical k values are obtained showing that bonding effects become negligible. The increase of the scale factors at the highest cut-off angles is not fully understood, but seems to be attributable to the decreasing numbers of observations and the increasing correlation between k and the second cumulants (*e.g.* the tails of the f curves become more and more parallel).

Since the scale-factor curves in Fig. 2 do not allow a unique determination of k, an average value, $k = 1{\cdot}01$, was regarded as the most reliable estimate to be used in ensuing electron-property calculations. There is, however, an uncertainty of about 1% in k.

The changes of the agreement factors with increasing cut-offs are also considerable. The $R_{w.o.u.}$'s drop to 0·0121–0·0123 between cut-offs of 0·7–0·8 Å^{-1},

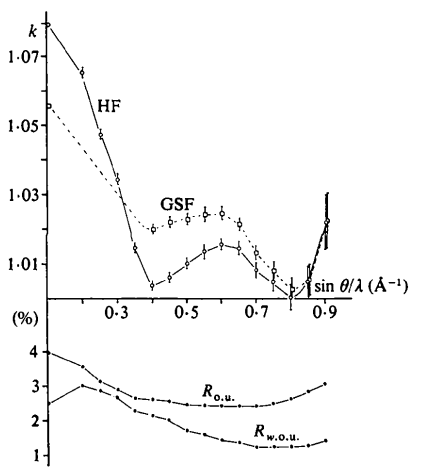

Fig. 2. Refined scale factor k (HFIAM and GSFIAM) and agreement factors (HFIAM) *versus* cut-off angle of data set.

reflecting the inadequacy of the spherically symmetric density distributions for the fit to all observed structure amplitudes or the actual electron density distribution. Observation of significant bond-density features could therefore be expected. The positional and thermal parameters from the all-data and the HO ($s \geq 0{\cdot}8$ Å^{-1}) refinements (both HFIAM and GSFIAM) are listed in Tables 4 and 5. As is to be expected from the similarity of the HF and GSF form factors at high $\sin\theta/\lambda$ values the results of the HO refinements of both models are identical. Furthermore, the vibrational parameters from the all-data refinements tend to accommodate bond-induced electron-distribution features. However, this is significantly less for the case of GSFIAM; related to the principal u_{ii} (HO) the r.m.s. deviations of u_{ii} (GSFIAM) are $13{\cdot}7 \times 10^{-4}$ Å^2 compared to $21{\cdot}4 \times 10^{-4}$ Å^2 for HFIAM. The same applies, though to a much lesser extent to the positional parameters [$29{\cdot}4 \times 10^{-5}$ (HFIAM) and $24{\cdot}8 \times 10^{-5}$ (GSFIAM) in fractional coordinates].

The comparison of the interatomic distances (Table 6) derived from the various refinements does not give any significant indications of atomic polarizations. The GSFIAM results are omitted since they do not add any further information.

(*b*) *Multipole refinements*

As a first step, all-data refinements (HFM-1 and GSFM-1) were carried out allowing only the coordinates and the monopole functions to vary while the core populations and the vibrational parameters obtained

Table 4. *Fractional coordinates* ($\times 10^5$) *with e.s.d.'s in parentheses* (*upper row HF, lower row GSF*)

		HFIAM GSFIAM	HO(0·8)	HFM-4 GSFM-4
Li	x	43289 (25)	43311 (18)	43341 (6)
		43293 (19)	43311 (18)	43339 (6)
	y	21465 (36)	21407 (19)	21425 (8)
		21439 (28)	21408 (19)	21430 (8)
	z	34402 (25)	34436 (17)	34399 (6)
		34451 (19)	34436 (17)	34396 (6)
B	x	12450 (14)	12425 (6)	12426 (3)
		12443 (11)	12425 (6)	12420 (4)
	y	67543 (17)	67522 (6)	67517 (3)
		67555 (14)	67523 (6)	67518 (4)
	z	27251 (14)	27224 (6)	27218 (3)
		27252 (11)	27224 (6)	27225 (4)
O(1)	x	8460 (9)	8458 (5)	8457 (3)
		8446 (7)	8458 (5)	8463 (4)
	y	35530 (12)	35557 (4)	35555 (3)
		35542 (9)	35557 (4)	35557 (3)
	z	25919 (10)	25883 (5)	25891 (4)
		25919 (8)	25883 (5)	25888 (4)
O(2)	x	35465 (9)	35459 (4)	35468 (3)
		35455 (7)	35459 (4)	35465 (3)
	y	77462 (11)	77427 (4)	77436 (3)
		77446 (9)	77427 (4)	77434 (3)
	z	31699 (9)	31682 (4)	31683 (3)
		31708 (7)	31682 (4)	31683 (3)

Table 5. *Thermal parameter* u_{ij} (Å^2 ×10^5) *with e.s.d.'s in parentheses (upper row HF, lower row GSF)*

		HFIAM GSFIAM	HO(0·8)	HFM-4 GSFM-4
Li	u_{11}	1233 (54)	1054 (29)	1063 (13)
		1100 (41)	1054 (29)	1045 (12)
	u_{22}	1557 (62)	1324 (19)	1338 (14)
		1489 (48)	1322 (18)	1334 (12)
	u_{33}	1997 (69)	1624 (27)	1684 (16)
		1909 (53)	1624 (27)	1660 (12)
	u_{12}	9 (49)	20 (16)	31 (10)
		65 (37)	21 (16)	35 (9)
	u_{13}	741 (51)	639 (22)	652 (12)
		714 (39)	639 (22)	641 (9)
	u_{23}	−7 (55)	9 (18)	15 (12)
		−11 (42)	10 (18)	15 (10)
B	u_{11}	1007 (28)	654 (11)	680 (7)
		897 (22)	645 (11)	661 (6)
	u_{22}	659 (22)	518 (8)	527 (5)
		588 (17)	508 (8)	520 (4)
	u_{33}	1376 (31)	1353 (10)	1408 (7)
		1366 (24)	1344 (10)	1386 (7)
	u_{12}	2 (19)	−24 (4)	−21 (4)
		3 (15)	−24 (4)	−22 (4)
	u_{13}	549 (24)	467 (7)	430 (4)
		523 (19)	464 (7)	469 (4)
	u_{23}	−4 (20)	−14 (4)	−11 (4)
		2 (16)	−14 (4)	−10 (4)
O(1)	u_{11}	949 (19)	782 (9)	768 (6)
		852 (14)	789 (9)	780 (4)
	u_{22}	567 (15)	416 (6)	441 (4)
		528 (12)	422 (6)	443 (3)
	u_{33}	2725 (30)	2545 (11)	2588 (9)
		2600 (23)	2552 (11)	2578 (7)
	u_{12}	−55 (15)	−39 (4)	−39 (4)
		−39 (12)	−39 (4)	−42 (3)
	u_{13}	842 (19)	751 (7)	777 (5)
		803 (15)	754 (7)	773 (4)
	u_{23}	−6 (18)	−9 (5)	−12 (5)
		2 (14)	−9 (5)	−11 (3)
O(1)	u_{11}	866 (18)	674 (8)	679 (6)
		776 (14)	681 (8)	690 (4)
	u_{22}	973 (17)	794 (7)	806 (5)
		908 (13)	801 (7)	811 (4)
	u_{33}	1581 (22)	1411 (8)	1450 (7)
		1491 (17)	1418 (8)	1448 (5)
	u_{12}	−154 (22)	−153 (4)	−154 (5)
		−145 (12)	−153 (4)	−151 (3)
	u_{13}	574 (17)	509 (6)	530 (5)
		536 (13)	512 (6)	530 (3)
	u_{23}	−86 (18)	−94 (4)	−96 (5)
		−83 (14)	−94 (4)	−94 (3)

Table 6. *Interatomic distances* (Å) *and angles* (°) *with e.s.d.'s in parentheses*

	HFIAM	HO(0·8)	HFM-4 = GSFM-4
B–O(1)	1·410 (2)	1·407 (1)	1·407 (1)
B–O(1^{iv})	1·392 (2)	1·392 (1)	1·393 (1)
B–O(2)	1·323 (1)	1·324 (1)	1·325 (1)
Li–O(1)	1·968 (2)	1·970 (1)	1·972 (1)
Li–O(2)	2·473 (1)	2·474 (0)	2·474 (0)
Li–O(2^{i})	1·960 (1)	1·959 (0)	1·960 (0)
Li–O(2^{ii})	2·007 (1)	2·006 (0)	2·006 (0)
Li–O(2^{iii})	1·945 (2)	1·946 (1)	1·942 (1)
O(1)–B–O(2)	117·55 (10)	117·47 (1)	117·50 (1)
O(1)–B–O(1^{iv})	115·78 (13)	115·92 (5)	115·91 (4)
O(2)–B–O(1^{iv})	126·66 (9)	126·60 (3)	126·57 (2)
O(1)–Li–O(2)	62·30 (6)	62·18 (2)	62·19 (2)
O(1)–Li–O(2^{i})	96·00 (7)	96·05 (3)	95·97 (3)
O(1)–Li–O(2^{ii})	112·64 (9)	112·69 (3)	112·52 (3)
O(1)–Li–O(2^{iii})	128·97 (8)	128·78 (3)	128·98 (3)
O(2)–Li–O(2^{i})	158·13 (6)	158·00 (2)	158·00 (2)
O(2)–Li–O(2^{ii})	93·69 (4)	93·64 (1)	93·62 (2)
O(2)–Li–O(2^{iii})	88·33 (4)	88·27 (1)	88·34 (1)
O(2^{i})–Li–O(2^{ii})	97·64 (4)	97·84 (1)	97·73 (2)
O(2^{i})–Li–O(2^{iii})	105·15 (6)	105·14 (2)	105·23 (2)
O(2^{ii})–Li–O(2^{iii})	109·83 (6)	109·85 (2)	109·95 (2)

Symmetry operations

(i) $x, y-1, z$ (iii) $1-x, y-\frac{1}{2}, \frac{1}{2}-z$

(ii) $1-x, 1-y, 1-z$ (iv) $-x, \frac{1}{2}+y, \frac{1}{2}-z$

Table 7. *Formal atomic net charges* (e) *from monopole populations*

	HFM-1 GSFM-1	HFM-2 GSFM-2	HFM-3 GSFM-3	HFM-4 GSFM-4
Li	0·35 (44)	0·72 (30)	1·24 (29)	1·20 (27)
	0·75 (44)	1·94 (30)	2·27 (28)	1·75 (29)
B	0·60 (20)	0·27 (11)	0·36 (10)	0·35 (12)
	1·03 (20)	0·77 (12)	0·74 (13)	0·59 (14)
O(1)	−0·47 (10)	−0·41 (4)	−0·62 (5)	−0·54 (6)
	−0·87 (11)	−1·38 (10)	−1·54 (15)	−1·20 (18)
O(2)	−0·50 (10)	−0·58 (7)	−0·98 (7)	−1·01 (8)
	−0·91 (11)	−1·33 (10)	−1·46 (18)	−1·15 (21)

from HO(0·8) were kept fixed. Each atom was given two monopole functions: $r'^2\exp(-\alpha_p^{st} r')$ and $r'^3 \times \exp(-\alpha_{p0} r')$, with fixed standard molecular exponents α_p^{st} (= $2\xi_p$) taken from the calculations of Hehre, Stewart & Pople (1969) and with the variable α_{p0} initially set equal to α_p^{st}.

Results are given in Tables 3 and 7. The R values dropped to HFM-1: 0·0273 (0·0169) and GSFM-1: 0·0271 (0·0170), expressing significant improvements of the models. This is especially true for HFM-1, and the atomic net charges obtained from the monopole populations approach those already employed in GSFM-1 (Li: +0·967, B: +0·915, O: −0·915) and not being significantly changed in GSFM-1. According to Fig. 3 this step shows that both models are already

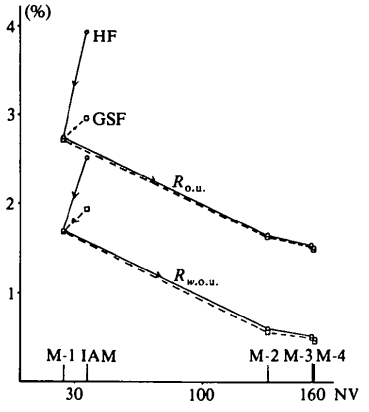

Fig. 3. Agreement factors (%) of HF and GSF models *versus* number of variables.

virtually equivalent in terms of statistical agreement. This finding means that the advantage of GSFIAM over HFIAM (analysis on IAM level) is almost exclusively due to the charge transfer obtained in the diatomic-molecule calculations. As soon as the monopoles in HFM-1 are allowed to reshape the still spherically symmetric atomic density distributions according to the observations the difference between the two models becomes marginal.

In the next step of the refinements the multipole functions of higher order were allowed to expand. The radial functions allocated were:

$$l = 1: \quad r'^2 \exp(-\alpha_{p1} r')$$

and

$$l > 1: \quad r'^l \exp(-\alpha_{pl} r'),$$

α_{p1}, α_{pl} again starting at α_p^{st}.

Since all atoms in $LiBO_2$ occupy general positions no constraints for the multipoles had to be considered, and consequently the number of subsidiary parameters for each atom was 31 (5 α values, 2 monopole and 24 higher multipole coefficients). This step brought about a decisive improvement of both models, indicated by R-value drops to HFM-2: 0·0163 (0·0060) and GSFM-2: 0·0161 (0·0056).

In HFM-3 and GSFM-3 the vibrational parameters were released in order to allow readjustment of the previously established u_{ij} (HO). Finally, the core populations were also released, but were tied together in the ratio of the initially assumed numbers of electrons of each atom. Thus only one more variable was added which corresponds to an adjustment of the scale factor. As in all previous steps the refinements were stopped when the parameter shifts were below $0{\cdot}5\sigma$, and the final agreement factors were HFM-4: 0·0148 (0·0047) and GSFM-4: 0·0146 (0·0046).*

Note that the estimated scale factor from GSFM-4 is 1·010 (13), in excellent agreement with the scale factor established in the HO refinement, suggesting that this scale factor is probably correct. The readjustment of the scales in the last step went along with a readjustment of the u_{ij}. Their corresponding final values from HFM-4 and GSFM-4 are in very good agreement, and also the agreement with the HO results is good, except for changes in u_{33} which exceed the sums of the associated e.s.d.'s by at most three times. If we apply again the r.m.s. discrepancy criterion to the principal u_{ii} (HO *versus* HFM-4 and GSFM-4) we find values of $3{\cdot}2 \times 10^{-4}$ Å^2 (HFM-4) and $2{\cdot}2 \times 10^{-4}$ Å^2 (GSFM-4) ($1{\cdot}6 \times 10^{-4}$ and $1{\cdot}3 \times 10^{-4}$ Å^2 omitting Δu_{33}).

* A list of observed and calculated structure factors (based on the final HFM-4 refinement) has been deposited with the British Library Lending Division as Supplementary Publication No. SUP 38254 (10 pp.). Copies may be obtained through The Executive Secretary, International Union of Crystallography, 5 Abbey Square, Chester CH1 2HU, England.

The results obtained so far lead to the following conclusions:

(i) The scale factor found with the pseudoatom refinement is consistent with the high-order result.

(ii) The first and second cumulants of the atoms can be regarded as well established. The overall agreement of the final vibrational parameters with those obtained from the HO refinements reflects a successful separation of bond-induced electron redistribution and vibrational smearing. It also proves once more the usefulness of the latter refinements.

(iii) The GSF model based on wavefunctions of diatomic systems is preferable on the independent-atom level. Also for multipole refinements it seems to be slightly superior to the HF model, indicated by all relevant parameters: scale factor, R values, GOF's *etc.*, at all refinement levels.

(iv) However, differences in the final model parameters of both refinements are small and hardly significant. This applies also to the final atomic net charges, with the exception of O(1). All other values (Table 7) agree within the limits of uncertainty. Compared to the numbers of electrons per atom obtained from the diatomic-systems calculations, the refined charge values imply the B atom to be less positively charged, the O atoms to carry more negative charge and, finally, the Li atom to be even more positive than Li^+. However, the shortcomings of formal net-charge determination by monopole population analysis have been mentioned above. In any case, the results show that the concept of $Li^+_\infty[BO_2]^-_\infty$ is rather more realistic than any model involving Li–O interactions of other than purely electrostatic nature. This is what we can infer from the refinement results so far. Other net-charge values can be expected from direct-space calculations (integrations or summations over charged volume elements) with reasonably defined atom volumes.

Finally, as an example of the model fit to the observations, Fig. 8(*a*) depicts the residual density distribution, $\rho(\mathbf{r})_{obs} - \rho(\mathbf{r})^{mult}_{calc}$, in the plane through Li, O(1), and O(2), showing merely statistical noise.

Electron densities and electrostatic properties

With the refined model parameters (HFM-4) difference Fourier maps were calculated according to Stewart (1979). The scale factor was chosen to be 1·01 as discussed above.

(*a*) *Dynamic deformation density*

$$\rho_{dyn}(\mathbf{r}) = \frac{2}{V} \sum_{h} \Delta F(\mathbf{h}) \cos 2\pi \mathbf{hr} \qquad (1)$$

with

$$\Delta F(\mathbf{h}) = k\,|F(\mathbf{h})_{obs}| \exp[i\varphi(\mathbf{h})^{mult}_{calc}] - F(\mathbf{h})^{IAM}_{calc}. \qquad (2)$$

Thus the reference density is the one obtained by superimposing the spherically symmetric densities of the independent atoms located at the proper positions. In principle any observed deformation density is the result of chemical bonding. The same holds for (*b*) and (*c*).

(*b*) *Dynamic deformation potential*

$$\Delta\Phi_{\rm dyn}(\mathbf{r}) = \frac{2}{\pi V}\sum_{h}[-\Delta F(\mathbf{h})/|\mathbf{h}|^2]\cos 2\pi\mathbf{hr}. \quad (3)$$

(*c*) *Dynamic deformation electric field*

$$\Delta\mathbf{E}_{\rm dyn}(\mathbf{r}) = \frac{-4i}{V}\sum_{h}[\mathbf{h}\Delta F(\mathbf{h})/|\mathbf{h}|^2]\cos 2\pi\mathbf{hr}. \quad (4)$$

Since (4) is a vector map, an informative representation is difficult. If required, the problem can be solved by plotting the distribution both of $|\Delta\mathbf{E}|$ and of the vectors $\Delta\mathbf{E}$ projected into the plane of interest.

(*d*) *Static deformation density*

The subsidiary parameters, *e.g.* the p sets of monopoles and higher multipoles which represent charge distributions in analytical descriptions, can be used to perform direct-space calculations of the static deformation density distribution:

$$\Delta\rho_{\rm stat}(\mathbf{r}) = \sum_{\rm sym}\sum_{p}[\rho(\mathbf{r}-\mathbf{R}_p)_p - \rho(|\mathbf{r}-\mathbf{R}_p|)_p^{\rm IAM}], \quad (5)$$

where $\rho(\mathbf{r}-\mathbf{R}_p)_p$ is a pseudoatom density in the asymmetric unit and $\rho(|\mathbf{r}-\mathbf{R}_p|)_p^{\rm IAM}$ is the IAM density at site p. In contrast to the Fourier summations, it is of course also possible here to represent deformations associated with single molecules, atoms, or selected multipoles alone.

Results

The BO_2 *chain*

Pauling (1948) has described the mixed nature of the B–O bonds in BO_3 groups. Owing to the electronegativity difference of 1·4 partial ionic character has to be considered, rendering the B atom positively and the O atoms negatively charged. This aspect is supported by the signs of the formal net charges (Table 7) derived from the monopole analyses at the various steps of the multipole refinements, as well as by the zeroth moments calculated for the diatomic system. From the covalent radii of B and O Pauling concluded that the bonds can be characterized as a resonance between single and double bonds with varying double-bond character according to the different bond lengths observed. If the bond-length–bond-strength relationship as applied by Zachariasen (1963) is considered, the three B–O bonds found in this work correspond to bond strengths of B–O(2) 1·12, B–O($1^{\rm iv}$) 0·94, and B–O(1) 0·905. Assuming that a stronger (shorter) bond displays a more prominent charge accumulation on the bond than a weaker one, one could expect to find the above bond-strength order at least qualitatively reproduced in the deformation density distribution.

Figs. 4(*a*) and 4(*b*) show the dynamic and static density distributions in the BO_3 plane, both derived from the HF model. The static deformation density distribution displays the features more pronouncedly, but does not add significant new ones which suggests that vibrational smearing and charge redistribution are separated successfully by use of the pseudoatom model. For another comparison the static deformation density obtained from the results of GSFM-4 is depicted in Fig. 4(*c*); this leads to the conclusion that both models yield essentially identical information about the charge redistribution. Therefore, all following property maps are based on HFM-4 results.

The highest density peaks (0·6–0·7 e Å^{-3}) show up on the short terminal bond B–O(2) (1·325 Å) and on the long B–O(1) bond (1·407 Å) whereas the slightly shorter B–O($1^{\rm iv}$) bond (1·392 Å) is associated with a significantly lower and more diffuse charge accumula-

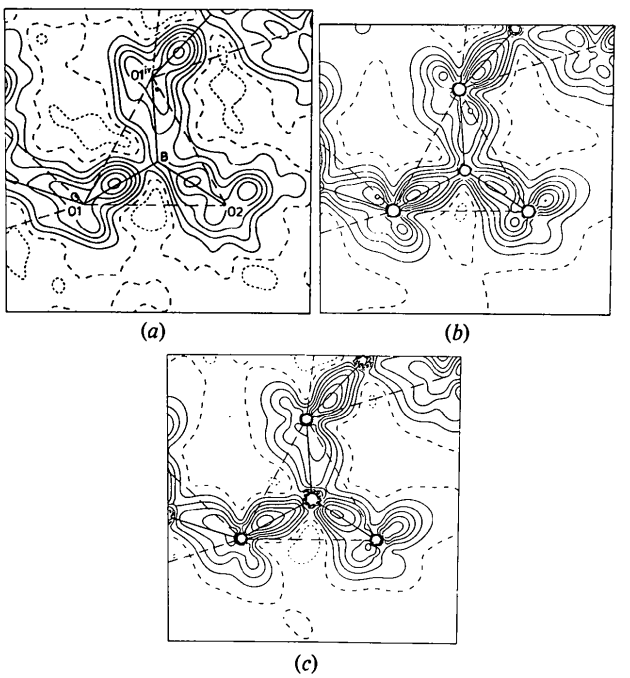

Fig. 4. Deformation densities in the plane of O(1), O($1^{\rm iv}$), O(2) and B. (*a*) Dynamic deformation density (HF), $\Delta\rho(F_o - F_c^{\rm IAM})$, (*b*) static deformation density (HF), (*c*) static deformation density (GSF). Contours in all plots are at intervals of 0·1 e Å^{-3}; negative contours are dotted, and the zero line is broken.

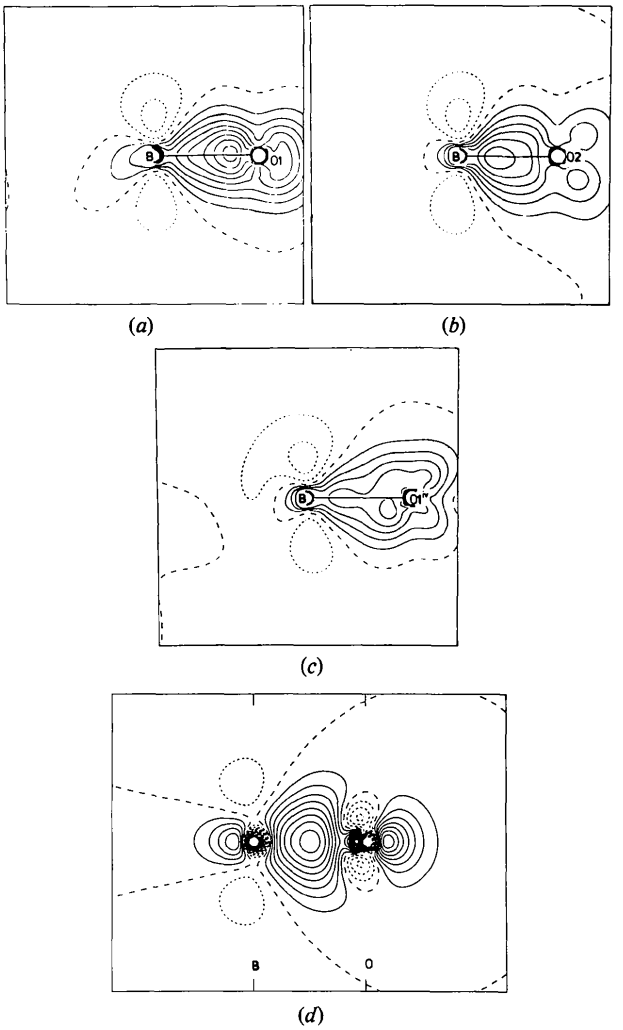

Fig. 5. Static deformation densities (HF) along the B–O bonds and perpendicular to the plane defined in Fig. 4. (*a*) B–O(1), (*b*) B–O(2), (*c*) B–O(1^{iv}), (*d*) theoretical deformation density distribution of the diatomic molecule BO. Contours are as in Fig. 4.

tion. This also becomes clear from Figs. 5(*a*), 5(*b*) and 5(*c*) which depict the static deformation density distributions perpendicular to the BO_3 plane and along the different B–O bonds. While B–O(1) and B–O(2) are qualitatively similar, B–O(1^{iv}) is distinctly different. Its deformation density is not only lower but also lacks the degree of symmetry with respect to the bond directions as displayed by the two former bonds. The similarity between Figs. 5(*a*), 5(*b*) and 5(*c*), which depict the static deformation density distribution of the diatomic B–O system obtained from *ab initio* calculations, may also be noted. In particular the quadrupole deformation associated with the B atom is well reproduced. Sections through the midpoints of the B–O bonds and perpendicular to them (Figs. 6*a*, 6*b* and 6*c*) also show the differences in the bonds clearly. If the thermal motion is properly described by the atomic vibrational parameters, the shapes of the deformation densities around B–O(1) and B–O(2) indicate more than just σ-type bonding, whereas that of B–O(1^{iv}) possesses almost full rotational symmetry. In addition to these striking differences, the charge distribution around O(1) in the BO_3 plane resembles that around O(2), with its clearly developed 'lone-pair-electron' regions, and this finding suggests that the B–O(1^{iv}) bond is formed by interaction between an sp^2 hybrid orbital of B (see Fig. 7) and the 'lone-pair-like' charge accumulation approximately perpendicular to the B–O(1) bond. The chains can then be considered as being polymerized from BO_2 anions [compare $(HBO)_n$, metaboric acid with a 120° O–B–O angle] which are arranged in such a way that the third 'free'

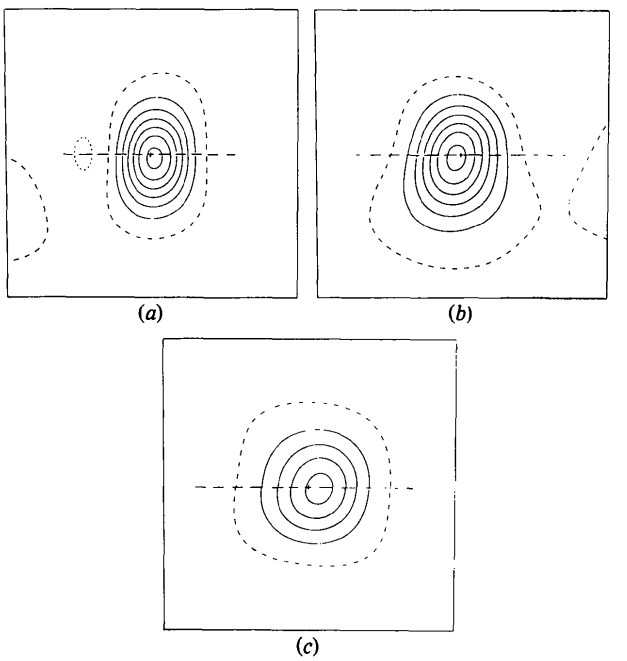

Fig. 6. Static deformation densities (HF) normal to and through the midpoints of the B–O bonds. (*a*) B–O(1), (*b*) B–O(2), (*c*) B–O(1^{iv}). Contours are as in Fig. 4.

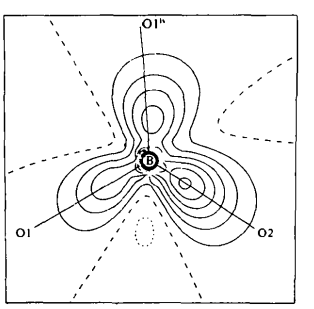

Fig. 7. Static deformation density (HF) in the plane defined in Fig. 4 calculated from the boron multipole expansion alone. Contours are as in Fig. 4.

sp^2 orbital of B can overlap with a $2p$ orbital of O(1). It is the recognition of the $O^{-B}{}_{-O}$ unit in the deformation density map which suggests this very simple but obvious model of chemical bonding in the $[BO_2]_\infty^{-\infty}$ chains.

Thus, we find two apparently strong bonds in $O^{-B}{}_{-O}$ and a weaker one connecting adjacent units. However, the two strong B—O bonds are of rather different lengths, and combining the deformation density distributions of Figs. 5 and 7 there is another difference between the two. For B—O(2) it seems that a strong sp^2 orbital contributes the major part of the bond density, while for B—O(1) the situation is reversed. Here, O(1) contributes more than B. But this may be an artifact due to the redundancy of the description of the charge density in the multipole model, and more evidence would be needed to establish such a distinction. However, the bond-length difference could be understood if we assume that O(2) is more negatively charged than O(1), so that the ionic character of the B—O(2) bond is larger than that of B—O(1). Also, if the crude model developed so far is of any value, one would expect the terminal O(2) to carry a greater negative formal charge than the bridging O atom. Indeed, the HF results do support this view. The GSF results do not, but here one can argue that the model has been biased by the populations $P_{p,\text{core}}$ employed. Very similar bond distances (1·326, 1·385, 1·401 Å) occur in the isotypic structure of $Ca(BO_2)_2$ (Marezio *et al.*, 1963*a*). For other metaborates like $NaBO_2$ (Marezio, Plettinger & Zachariasen, 1963*b*) the situation is different. Here there are only two different B—O bonds, the terminal B—O bond being even shorter (1·280 Å) and the bridging bond even longer (1·433 Å), so that the mechanisms for the linking of the BO_2 units are somewhat different.

Deformation densities comparable to those in $LiBO_2$ have been observed recently in $Li_3B_5O_8(OH)_2$ (Shevyrev, Muradyan, Simonov, Egorov-Tismenko, Simonov & Belov, 1981), and this applies as well to the Li—O 'bond' discussed next.

The Li *atom*

At first sight the situation around Li is characterized by coordination of five O atoms, of which four, O(1), $O(2^{I})$, $O(2^{II})$, and $O(2^{III})$, form a distorted tetrahedron with Li—O distances of 1·945–2·007 Å, mean 1·97 Å, in agreement with the sum of the ionic radii of $^{IV}Li^+$ and $^{IV}O^{2-}$ (1·97 Å) (Shannon & Prewitt, 1969). It also compares well with the theoretically optimized Li—O distance in $Li(OH)_4^{3-}$ (Gibbs, Meagher, Newton & Swanson, 1981). The mean bond angle around Li is 108·37 (3)°. However, the Li atom is only 0·095 (1) Å from the face defined by O(1), $O(2^{I})$, and $O(2^{II})$, so that one can also speak of a half-sphere of coordination. The O(2)—Li distance is almost 2·5 Å (Table 6) and, hence, it can be assigned to the next LiO_4 tetrahedron. Each O(2) is a vertex common to the three LiO_4 tetrahedra which connect the staggered BO_2 chains.

Figs. 8(*b*) and 8(*c*) show the dynamic and static deformation density distributions in the plane defined by Li, O(1), O(2), with $O(2^{I})$ lying almost in that plane too. Neither map shows any significant charge redistribution associated with Li or its diffuse $2s$ electron. The 'lone-pair' regions of O(1) and O(2) are oriented towards Li with a distinct asymmetry in the distribution around O(2), which clearly favours the short $Li—O(2^{I})$ distance. The amount of charge accumulation in the vicinity of O(2) along the $O(2^{I})$—Li bond direction suggests that the $2s$ electron of Li is predominantly transferred to the terminal O(2), yielding the density distribution along $O(2^{I})$—Li similar to

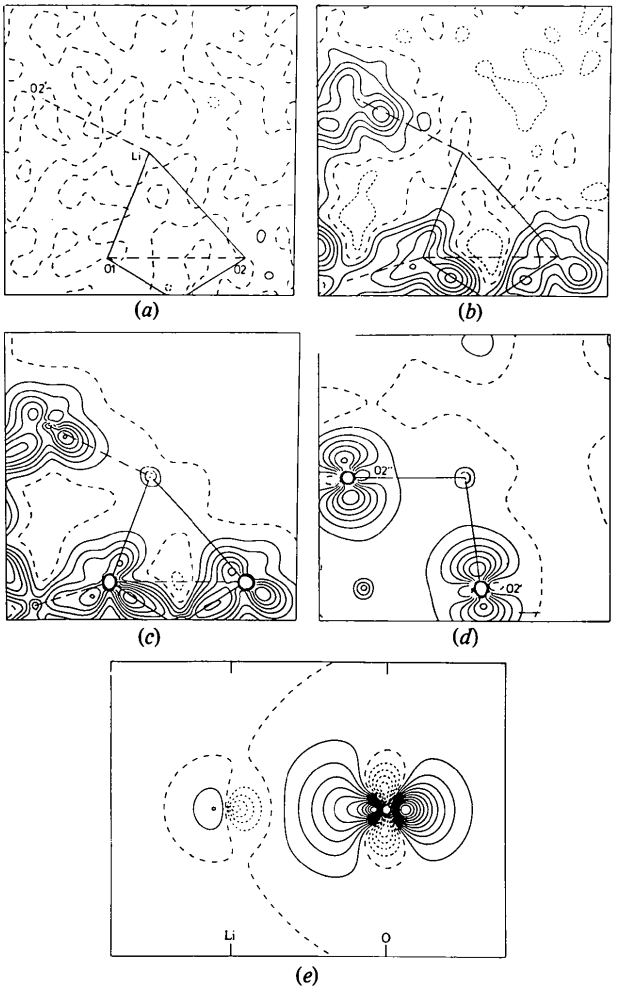

Fig. 8. (*a*)–(*c*) Deformation densities in the plane of O(1), O(2), Li: (*a*) residual density, $\Delta\rho(F_o - F_c)$, after refinement HFM-4, (*b*) dynamic deformation density (HF), $\Delta\rho(F_o - F_c^{\text{IAM}})$, (*c*) static deformation density (HF). (*d*) Static deformation density (HF) in the plane through $O(2^{I})$, Li, $O(2^{II})$. (*e*) Theoretical deformation density distribution of the diatomic molecule LiO. Contours are as in Fig. 4.

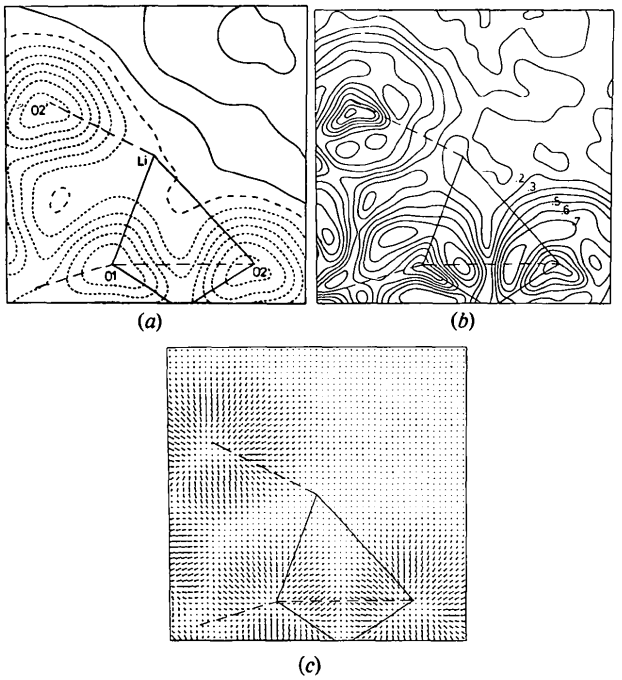

Fig. 9. (*a*) Deformation potential, $\Delta\Phi(F_o - F_c^{IAM})$, and (*b*) magnitude of the deformation electric field, $|\Delta\mathbf{E}(F_o - F_c^{IAM})|$, (*c*) projection vectors $\Delta\mathbf{E}$ in the plane O(1), O(2), Li. Vectors are normalized to prevent overlap. Contours are as in Fig. 4.

the theoretical distribution for the Li–O diatomic system (compare especially Figs. 8*d* and 8*e*). The angle B–O(2^{I})–Li is 121·10 (3)°, well within the range of bond angles around O atoms in organic compounds. Since the corresponding lobes on the two symmetry-related O atoms, O(2^{II}) (see Fig. 8*d*) and O(2^{III}), are oriented towards 'their' Li atoms and stand perpendicular to the bonds drawn in Fig. 1, one can characterize the Li–O(2^{I}) bond as the most important one (compare also Amstutz, Dunitz & Seebach, 1981). The deformation potential distribution $\Delta\Phi$ in Fig. 9(*a*) and the deformation electric field (Figs. 9*b* and 9*c*) support this assumption. The potential contours around O(2^{I}) as well as the $|\Delta\mathbf{E}|$ contours and the $\Delta\mathbf{E}$ map projected on to the plane indicate the preference of the Li–O(2^{I}) bond. The deformation potential at O(2) is also somewhat lower than at O(1) which is another expression of the more negative formal net charge associated with O(2) as already found from the HF monopole population analysis. The positive contours in the upper right-hand corner of Fig. 9(*a*) are due to repulsion between the next BO_2 chains above and below the section (see Fig. 1).

Conclusions

Regarding the finally achieved agreement index $R_{w.o.u.} = 0{\cdot}0047$ as an indicator of the quality of both the data set and the description of the charge density distribution shows that the validity of the rigid pseudoatom model has been proved in the present study. This is demonstrated especially by the drastic gain of agreement obtained with the expansion of the higher multipoles in HFM-2 and GSFM-2. Subsequent minor decreases in the R values resulting from the release of certain crystallographic standard parameters indicate that these had been well established in the preliminary HO refinements ($s \geq 0{\cdot}8$ Å^{-1}). However, since the R values of the HO refinements were larger than those of the first expansion of the higher multipoles, we must conclude that bond-induced density accumulations were scattering beyond the cut-off and/or that the scattering-factor curves of the neutral atoms themselves were not quite adequate for the description of the actual distribution of the core electrons. The former seems to be more probable considering the well localized charge accumulation on the Li–O(2^{I}) bond.

As to the use of the monopole terms of the generalized scattering factors derived from diatomic molecules, it can be stated that they are considerably superior to the HF scattering factors for neutral atoms on the conventional refinement level. This is because they introduce transferable bond information in terms of the charge transfer between the bonding partners of the diatomic system. The R value of GSFIAM is 24% lower than that of HFIAM (Table 3). A similar though smaller difference has been observed in a study on forsterite, Mg_2SiO_4 (Kirfel, Will & Stewart, 1982). Clearly, the degree of superiority depends on the ratio of valence to core electrons, and also on the electronegativity differences in the structure. It may be worthwhile to employ GSF's generally on the IAM level for light-atom structures, especially when atoms of widely differing electronegativities are involved. The advantage disappears, however, as soon as the monopole functions of the pseudoatom model are allowed to shape the isotropic components of the scattering factors.

Summing up the findings of the charge density distribution, especially the recognizability of features of the theoretically derived diatomic deformation density distributions, leads to a simple model of binding in the molecular unit $LiBO_2$, and in the giant molecule, the crystal (Fig. 10). Li forms a stable bond with O(2)

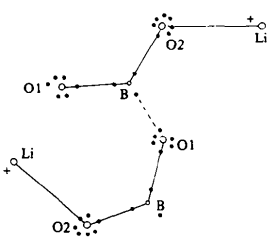

Fig. 10. Schematic drawing of the $LiBO_2$ binding model. Black dots represent valence electrons.

becoming about onefold positively charged due to the charge transfer. O(2), being also bonded to B, is then in a favourable electron-state condition. B also binds O(1); however, there is an unpaired electron left on O(1) which can then interact with another free electron of the B atom of the next unit, as discussed above. This interaction leads to the polymerization into chains, and the chains are then held together by the electrostatic forces between Li^+ cations and negatively charged O atoms. The model can also be expressed in terms of the bond-strength–bond-valence balance. The sum of the bond strengths of bonds involving B is 2·965, close enough to the valence number 3. For O(1) the sum is 1·845 and for O(2) only 1·12. Assuming that the differences from valence number 2 express the bond strengths of the Li–O(1) (0·155) and Li–O(2^I) (0·88) bonds, the bond-strength sum for Li is 1·035 – matching its valence number of 1 and supporting the importance of the Li–O(2^I) bond.

It must be emphasized here that this attempt to rationalize the chemical bonding in $LiBO_2$ was developed in a straightforward manner just by interpreting the information in the deformation density maps. Clearly, the situation is much more complicated and cannot be easily unravelled in terms of single bonds; but we consider this study to be an example of how knowledge about chemical bonding derived from calculations on diatomic systems can be used beneficially in interpretations of observations in more complex compounds.

This work has received support from the Deutsche Forschungsgemeinschaft which is gratefully acknowledged. One of us (AK) is indebted to the Carnegie–Mellon University for financial support during his stay at the Department of Chemistry, and wishes to express his gratitude to M. A. Spackman for many fruitful discussions. This research was also supported in part by NSF grant CHE-80-16165.

References

AMSTUTZ, R., DUNITZ, J. D. & SEEBACH, D. (1981). *Angew. Chem. Int. Ed. Engl.* **20**(5), 465–466.
BECKER, P. & COPPENS, P. (1974*a*). *Acta Cryst.* A**30**, 129–147.
BECKER, P. & COPPENS, P. (1974*b*). *Acta Cryst.* A**30**, 148–153.
BEHM, K. (1976). Theseis, Univ. Freiburg, Federal Republic of Germany.
BENTLEY, J. J. & STEWART, R. F. (1976). *Acta Cryst.* A**32**, 910–914.
CADE, P. E. & HUO, W. M. (1975). *At. Data Nucl. Data Tables*, **15**, 1–39.
CLEMENTI, E. (1965). *IBM J. Res. Dev.* **9**, 2.
GIBBS, G. V., MEAGHER, E. P., NEWTON, M. D. & SWANSON, D. K. (1981). *Structure and Bonding in Crystals*. Vol. I, pp. 195–225. London, New York: Academic Press.
HEHRE, W. J., STEWART, R. F. & POPLE, J. A. (1969). *J. Chem. Phys.* **51**, 2657–2664.
KIRFEL, A., GUPTA, A. & WILL, G. (1979). *Acta Cryst.* B**35**, 2291–2300.
KIRFEL, A., WILL, G. & STEWART, R. F. (1982). In preparation.
MAREZIO, M., PLETTINGER, H. A. & ZACHARIASEN, W. H. (1963*a*). *Acta Cryst.* **16**, 594–595.
MAREZIO, M., PLETTINGER, H. A. & ZACHARIASEN, W. H. (1963*b*). *Acta Cryst.* **16**, 594–595.
PAULING, L. (1948). *The Nature of the Chemical Bond*. Ithaca, New York: Cornell Univ. Press.
SHANNON, R. D. & PREWITT, C. T. (1969). *Acta Cryst.* B**25**, 925–946.
SHEVYREV, A. A., MURADYAN, L. A., SIMONOV, V. I., EGOROV-TISMENKO, Y. K., SIMONOV, M. A. & BELOV, N. V. (1981). *Sov. Phys. Dokl.* **26**(3), 251–253.
SPACKMAN, M. A. & STEWART, R. F. (1982). In preparation.
STEVENS, E. D. & COPPENS, P. (1975). *Acta Cryst.* A**31**, 612–619.
STEVENS, E. D. & COPPENS, P. (1976). *Acta Cryst.* A**32**, 915–917.
STEWART, R. F. (1979). *Chem. Phys. Lett.* **65**, 335–342.
STEWART, R. F., BENTLEY, J. J. & GOODMAN, B. (1975). *J. Chem. Phys.* **63**, 3786–3793.
ZACHARIASEN, W. H. (1963). *Acta Cryst.* **16**, 385–389.
ZACHARIASEN, W. H. (1964). *Acta Cryst.* **17**, 749–751.

Acta Cryst. (1983). B**39**, 185–189

Weak Asymmetry in β-Si_3N_4 as Revealed by Convergent-Beam Electron Diffraction

BY YOSHIO BANDO*

Center for Solid State Science, Arizona State University, Tempe, AZ 85287, USA

(*Received* 30 *July* 1982; *accepted* 25 *November* 1982)

Abstract

The thickness dependence of the apparent crystal symmetry in a pure β-Si_3N_4 crystal has been studied by the convergent-beam electron diffraction (CBED) technique. The [11$\bar{2}$0] zone-axis CBED pattern for a thin crystal is compatible with the centrosymmetric space group $P6_3/m$, while that for a thick crystal would require the non-centrosymmetric space group $P6_3$. The thickness dependence of this result is discussed on the basis of the crystal structure of β-Si_3N_4 with space

* Present address: National Institute for Research in Inorganic Materials, 1-Namiki, Sakura-mura, Niihari-gun, Ibaraki 305, Japan.

0567-7408/83/020185-05$01.50